Article

# A wearable in-sensor computing platform based on stretchable organic electrochemical transistors

Dingyao Liu[1,4], Xinyu Tian [1,4], Jing Bai [1,4], Shaocong Wang [1,4], Shilei Dai [1], Yan Wang [1], Zhongrui Wang [1,2] & Shiming Zhang [1,3]

Organic electrochemical transistors could be used in in-sensor computing and wearable healthcare applications. However, they lack the conformity and stretchability needed to minimize mechanical mismatch between the devices and human body, are challenging to fabricate at a scale with small feature sizes and high density, and require miniaturized readout systems for practical on-body applications. Here we report a wearable in-sensor computing platform based on stretchable organic electrochemical transistor arrays. The platform offers more than 50% stretchability by using an adhesive supramolecular buffer layer during fabrication that improves robustness at interfaces under strain. We fabricate stretchable transistor arrays with feature sizes down to 100 μm using a high-resolution six-channel inkjet printing system. We also develop a coin-sized data readout system for biosignal acquisition. We show that our coin-sized, smartwatch-compatible electronic module can provide wearable in-sensor edge computing.

The development of wearable computing devices for applications in remote healthcare monitoring and environmental sensing requires the integration of sensing and computing within a single hardware system[1–4]. Such in-sensor computing could, in particular, enhance the power efficiency of electronic systems[5,6]. Research on the integration of sensing and computing is progressing, but various challenges remain. One is how to create a hardware unit with mechanical stretchability and conformability[7–9], as motion artefacts caused by the mechanical mismatch between rigid hardware and the human body can affect the quality and reliability of gathered data[8].

Organic electrochemical transistors (OECTs) are promising devices for use in sensing[10], computing[11,12] and in-sensor computing applications[13]. The gate electrode of OECTs can be used to detect electrochemical signals of interest, and the OECT—as a whole—amplifies the signal[14]. OECTs are typically based on the conducting polymer poly (3,4-ethylenedioxythiophene):poly(styrenesulfonate) (PEDOT:PSS)[14]. Importantly, PEDOT:PSS OECTs can offer excellent biocompatibility

and water stability for up to 800 days[15], making them useful for practical wearable and implantable applications[16]. They can also work at low voltages (around millivolts) and maintain high sensitivity and computing efficiency[17].

A range of methods to incorporate OECTs in wearable applications have been developed[18], including transfer patterning[19], spray coating[20], microcracked thin gold (Au) films[21], pre-straining of substrates[22], laser printing[23], screen printing[24] and micropattern design[25–27]. Furthermore, these devices have been used in both sensing and computing applications. However, there are only a few reports on intrinsically stretchable OECTs (ISOECTs) being used in high-density integrated biocircuits[28,29]. Developing ISOECTs requires materials capable of serving as stretchable channels, electrodes, gel electrolytes and insulators, as well as the development of scalable manufacturing methods. System-level research that can validate the efficacy and reliability of the technology in practical scenarios is also needed.

[1]Department of Electrical and Electronic Engineering, The University of Hong Kong, Hong Kong SAR, China. [2]School of Microelectronics, Southern University of Science and Technology, Shenzhen, China. [3]State Key Laboratory of Pharmaceutical Biotechnology, The University of Hong Kong, Hong Kong SAR, China. [4]These authors contributed equally: Dingyao Liu, Xinyu Tian, Jing Bai, Shaocong Wang. ✉e-mail: zrwang@eee.hku.hk; beszhang@hku.hk
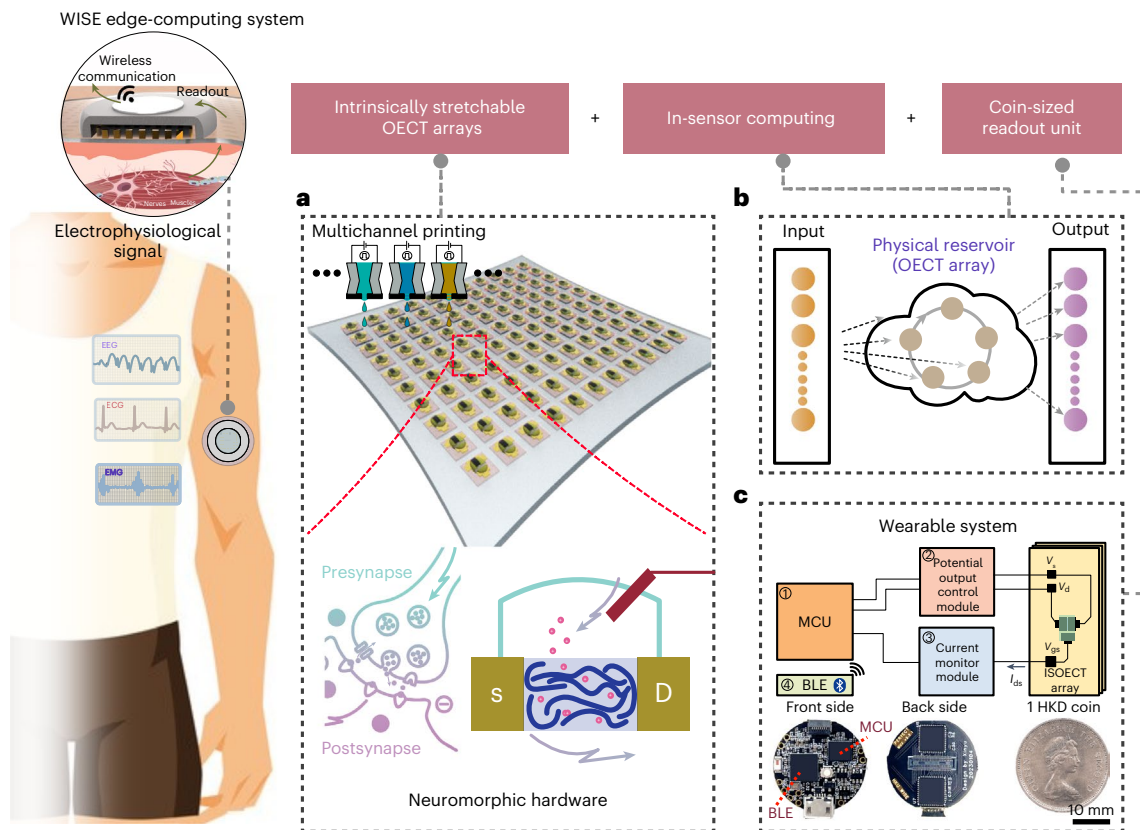
**Fig. 1 | Design strategy for coin-sized wearable in-sensor computing unit (WISE platform) based on ISOECT arrays. a–c**, The platform includes an inkjet-printed ISOECT array (**a**), an ISOECT-array-based RC network (**b**) and a miniaturized readout unit for wearable data acquisition and analysis (**c**).

In this Article, we report the scalable fabrication of micro-ISOECT arrays and their integration into a wearable integrated and soft electronic (WISE) platform (Fig. 1). The WISE platform is created by developing a standardized material protocol that provide OECTs with stretchability of greater than 50%. This is achieved by using an adhesive supramolecular buffer layer during fabrication to enhance strain-related robustness at interfaces. We use a high-resolution inkjet printing system with six channels, which provides the one-shot manufacturing of ISOECT arrays with a yield of over 95% and feature sizes of 100 μm. We also develop a coin-sized data readout unit that allows biosignals to be acquired and processed at source. We benchmark the performance of our WISE platform against existing platforms, illustrating its competitiveness in a range of applications.

## Stretchable OECT design

ISOECTs are designed with an in-plane structure consisting of a stretchable elastomeric substrate, a semiconducting polymer channel (PEDOT:PSS), a solid-gel electrolyte as the gating medium and Au source (S)/drain (D)/gate (G) electrodes (Fig. 2a). After identifying an optimal material solution for each functional layer as well as the whole assembly, we successfully endowed ISOECTs with a stretchability of 50% (sufficient to accommodate skin deformation) without major compromise on performance or stability.

To begin, we selected styrene–ethylene/butylene–styrene (SEBS), a common elastomer for stretchable electronics, as the substrate. For the electrodes, we used ultrathin Au films (thickness, 20 nm) to obtain intrinsic stretchability on the SEBS substrate[30]. Next, we used PEDOT:PSS as the channel material. PEDOT:PSS was selected for its excellent water stability and mixed ionic–electronic conductivity[31]. To enhance the stretchability and water stability of the PEDOT:PSS channel on SEBS, we introduced the crosslinker, poly(ethylene

glycol)diglycidyl ether (PEGDE), to replace the commonly used (3-glycidyloxypropyl)trimethoxysilane (GOPS). This is because PEGDE is a mechanically softer crosslinker than GOPS[32], which helps increase the stretchability of the PEDOT:PSS films (Supplementary Fig. 1). Additionally, we synthesized a tough adhesive polymer (TAP; Methods) as a buffer layer, the use of which can further improve the stretchability of the device by facilitating energy dissipation through autonomous breakage and reformation of dynamic bonds[33]. Besides, the dopamine (DA) group was grafted on the side chain of TAP molecules to improve their adhesion with PEDOT:PSS, preventing interlayer delamination (Fig. 2b–c and Supplementary Figs. 2 and 3). Last, we used an intrinsically stretchable ion gel composed of ionic liquids (ILs), polyacrylic acid (PAA) and poly(3-dimethyl (methacryloyloxyethyl) ammonium propane sulfonate) (PDMAPS), as the solid-state electrolytes. PDMAPS/PAA/ILs were chosen for their excellent ambient stability, printability[34] and biocompatibility (Supplementary Figs. 4–6), permitting their easy integration into ISOECTs.

Through the systematic material development, processing and assembling mentioned above, the performance of each layer was ensured within the targeted 50% strain range (Supplementary Figs. 3, 4, 7 and 8). The combined use of the soft crosslinker PEGDE and the TAP buffer layer was verified, leading to a minimal performance loss of ISOECTs under strain (Fig. 2d–g). The figure of merit of the resultant device is on par with those fabricated on silicon and plastic substrates. Specifically, the on/off ratios remained above $10^3$ under all the strain values, and the transconductance ($G_m$) exceeded 1 mS (width ($W$)/ length ($L$) = 2, $V_{gs}$ = 0.3 V). These results confirm the viability of the established material protocols. It is worth mentioning that using a SEBS substrate with low oxygen permeability is the key to ensuring a high on/off ratio of the ISOECTs. Details of materials processing are described in the Methods.
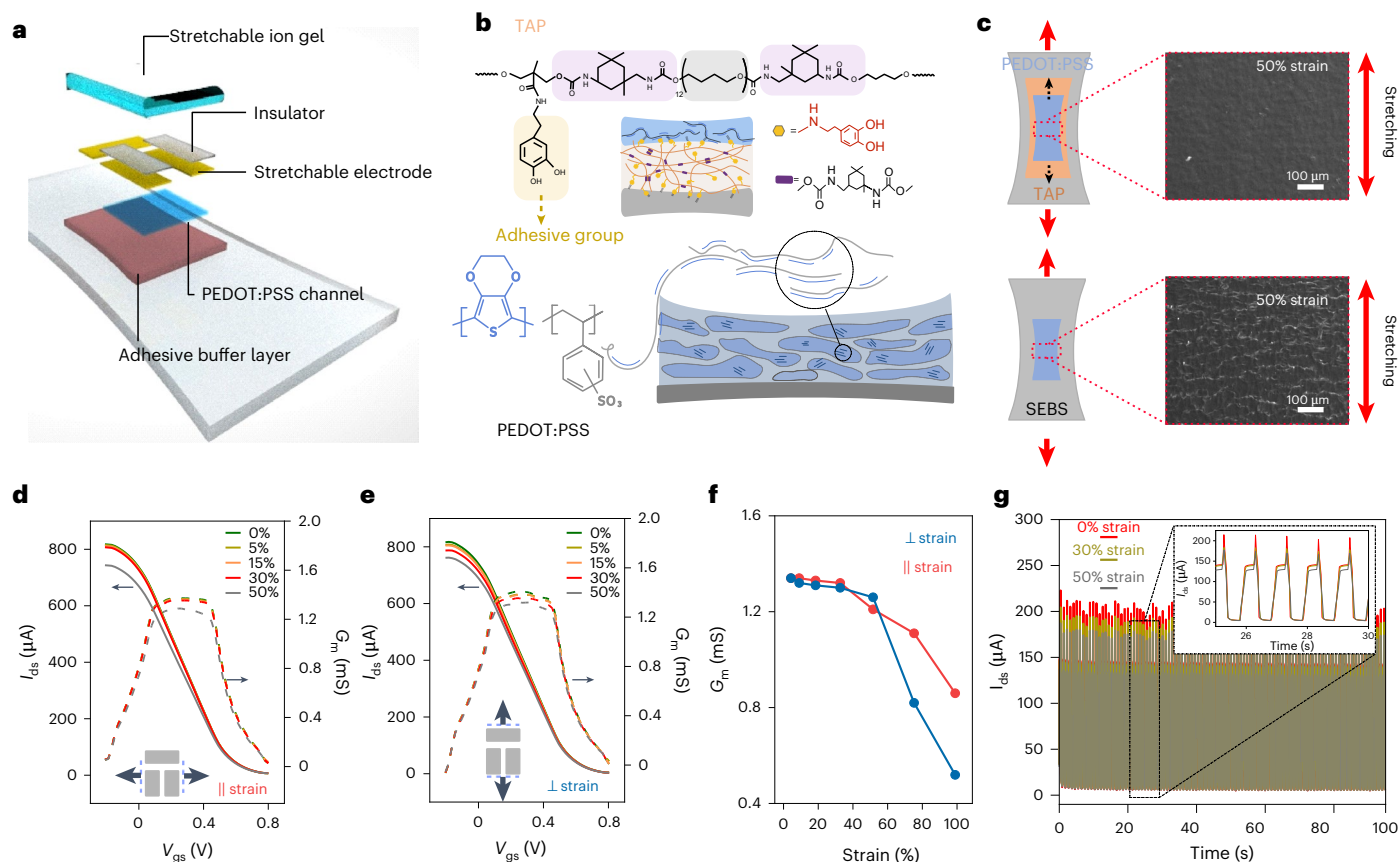
**Fig. 2 | Materials strategies for the ISOECT. a**, Illustration of the ISOECT structure. **b**, Chemical structure of the TAP molecules and their use as an adhesive buffer layer between the elastomeric substrate and PEDOT:PSS.

**c**, Scanning electron microscopy images of PEDOT:PSS films with and without TAP under 50% strain. **d–g**, Transfer curves, $G_m$ and transient responses of the ISOECT ($W = 500\ \mu m$, $L = 250\ \mu m$) at different strain values (0%–50%).

## Scalable fabrication of stretchable OECT array

The established material solutions permit the assembly of high-performing and robust ISOECT units, but constructing functional circuits requires high-density device arrays. However, compatibility issues arise when patterning those stretchable materials with conventional cleanroom techniques designed for rigid silicon electronics. For example, procedures such as annealing and lift-off of the photoresist can cause deformation and deterioration of elastomers and gels, affecting alignment, device yield and device-to-device uniformity.

To address the fabrication challenges, we developed a multichannel inkjet-printing-based platform (Supplementary Fig. 9). The process flow to fabricate ISOECT arrays is illustrated in Fig. 3a,b (detailed in the Methods). First, the ink of TAP was prepared by dissolving it in an ethanol/butyl acetate mixture, followed by printing it on the pre-prepared SEBS substrate as a buffer layer. Next, electrodes (S, D and G) made of ultrathin Au electrodes (20 nm) and interconnects were patterned with a shadow mask. Ink of silver nanowires was subsequently printed on the interconnect region to ensure high conductivity under strain (Supplementary Fig. 10). Alternatively, the stretchable interconnects and electrodes can also be fabricated by the direct inkjet printing of composited Au ink, but have to compromise on conductivity (Supplementary Fig. 11). Afterwards, filtered ink of PEDOT:PSS was printed as the channel (Supplementary Fig. 12). Finally, the ion-gel electrolyte was printed to bridge the gate electrode and channel.

The printing resolution achieved $100\ \mu m$ for all the functional layers, with a high device yield of 95% (Fig. 3c–f). With the established printing platform, we successfully printed a $10 \times 10$ ISOECT array within a $1.44\ cm^2$ area, sufficient for wearable sensing and computing applications. The metrics of the device unit, such as the on/off ratio

($>10^3$), mobility ($\sim$0.8 cm$^2$ V$^{-1}$ s$^{-1}$), $G_m$ ($\sim$1 mS) and stretchability (50%), were comparable with the reference device (Supplementary Fig. 13). Minimal device-to-device variations were achieved under different strain values, benefiting from the high uniformity and reliability of the printing process (Fig. 3g–j and Supplementary Fig. 14).

## Stretchable OECTs for neuromorphic computing

Having determined the materials solutions and fabrication protocols for ISOECT arrays, we subsequently explored their use as conformable, nonlinear and low-power neuromorphic computing hardware. To exploit the full potential of the ISOECT array, we adopted the reservoir computing (RC) framework, a promising machine learning algorithm known for its minimal requirements on computing resources and ability to operate with small training datasets (Fig. 4a)[35]. RC utilize neuron-like nonlinear hardware units in which OECTs excel. Structurally, OECTs resemble three-terminal transistors, where the gate electrode is analogous to the presynapse of a neuron, receiving input ionic signals, whereas the channel between the source and drain electrodes is analogous to a post-synapse, responding to the gate signals[36]. Operationally, the signals at the gate electrode propagate through nonlinear ionic transports via the electrolyte[37,38], modulating the channel conductance via a nonlinear electrochemical doping/dedoping process (Supplementary Fig. 15)[39]. Additionally, the inherent stretchability of ISOECT arrays favours their uses at soft biological interfaces.

To implement ISOECT arrays in the RC network, we first evaluated their potential in distinguishing drain currents ($I_{ds}$) as different digitalized gate inputs. We began by inputting four-bit pulse streams at the gate electrode and recording the corresponding output $I_{ds}$ (Fig. 4b), where '1' denotes applying a gate voltage (0.4 V) and '0' denotes no
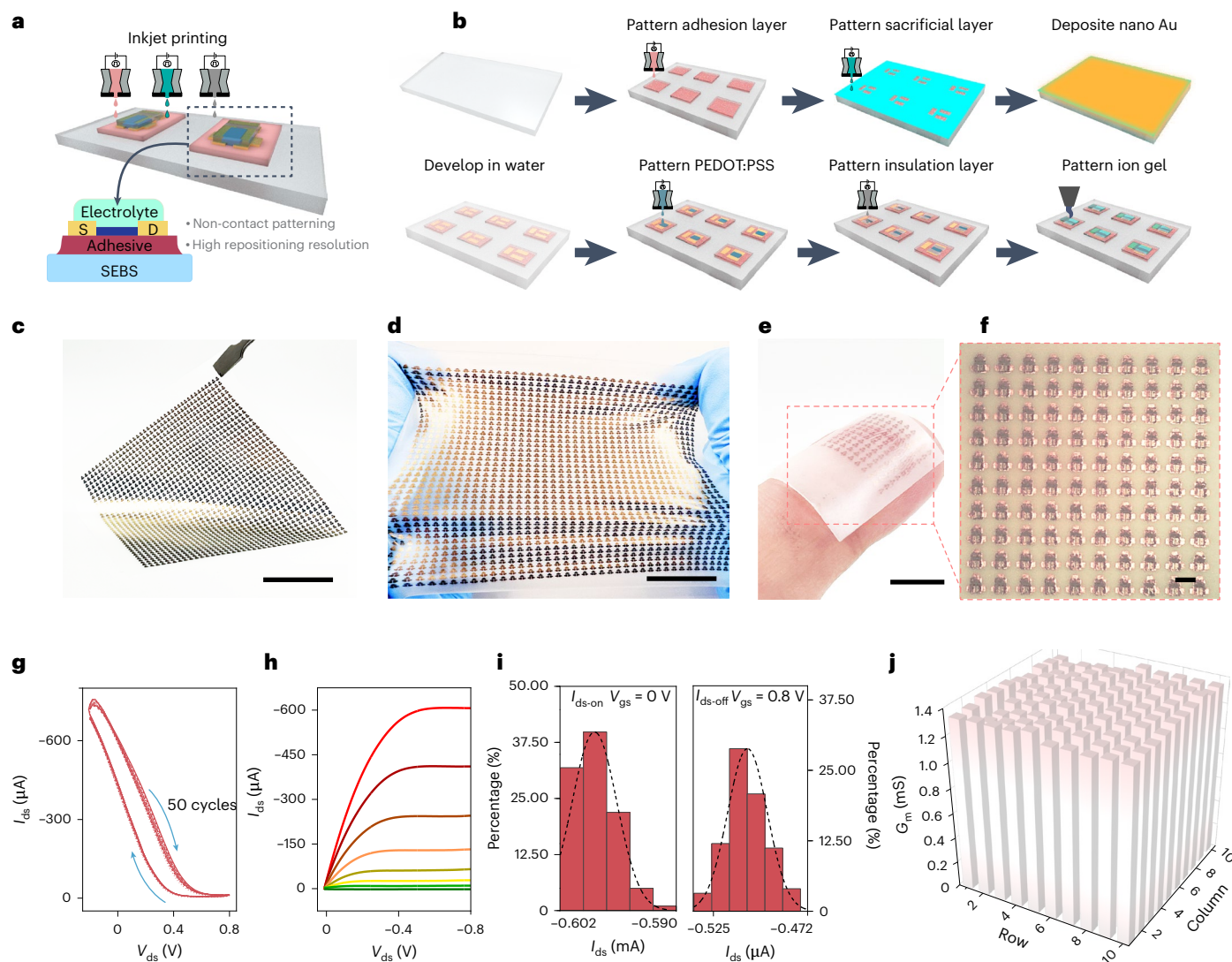
**Fig. 3 | Scalable fabrication of the ISOECT array. a**, Illustration of the multichannel inkjet printing of ISOECTs. **b**, Process flow of ISOECT array fabrication. **c,d**, Optical images of an ISOECT array containing 1,600 devices at 0% strain (**c**) and 50% strain (**d**). Scale bar, 1 cm. **e,f**, Optical image of ISOECT array (10 × 10) within an area of 1.2 cm × 1.2 cm ($W$ = 500 μm, $L$ = 100 μm). Scale bar, 1 cm. **g**, Transfer curves of ISOECTs for 50 cycles, with $V_{ds}$ fixed at −0.2 V and $V_{gs}$ scanned from −0.4 to 0.8 V. **h**, Output curves of ISOECTs, with $V_{ds}$ scanned from 0 to −0.8 V and $V_{gs}$ scanned from 0 to 0.8 V. **i**, Distribution of on-state and off-state currents of the ISOECT (10 × 10 array). **j**, Comparison of $G_m$ values between devices in the 10 × 10 array, indicating the high reliability of the fabrication process.

voltage is applied (0 V). As expected, when a single pulse was applied at the gate, $I_{ds}$ exhibited a nonlinear drop. The removal of the pulse caused $I_{ds}$ to nonlinearly return to its initial value. The application of multiple pulses led to a steeper drop in $I_{ds}$. Importantly, we observed distinguishable $I_{ds}$ values for all the 16 sequential pulse inputs, ranging from '0000' to '1111', benefiting from the excellent nonlinearity of ISOECTs. In other words, ISOECTs could generate 16 distinguishable analogue $I_{ds}$ values for the corresponding 16 sequential input states (Fig. 4c and Supplementary Figs. 16 and 17).

Subsequently, we explored the use of one ISOECT array to classify digits in an image (Fig. 4d). Each digit is composed of 20 pixels (black/white) arranged in five rows, with four pixels in each row. After converting the black/white pixels into sequential high-/low-voltage pulses and feeding them to the reservoir (that is, the ISOECT array), distinguishable $I_{ds}$ patterns were obtained (Fig. 4e,f). These patterns remained distinguishable under strain (Fig. 4g). We then further verified the capability of ISOECT for predicting handwritten digits from the Mixed National Institute of Standards and Technology dataset (Supplementary Fig. 18 and Methods). To facilitate processing, we first

binarized the handwritten characters to a 28 × 28 pixel² image (black/white), which was then converted into a 4 × 196 array that could be fed to the ISOECT reservoir. Each neuron of the reservoir was assigned a temporary $I_{ds}$ value of a corresponding ISOECT. The sparse connections of the readout map, which link the reservoir layer and the output layer, were optimized during the training process. Since only the sparse connection in the output layer needs to be trained, the above approach could significantly reduce data processing costs (Supplementary Figs. 19 and 20).

To visualize the distribution of the high-dimensional feature vectors encoded by the ISOECT reservoir, we used a principal component analysis to reduce them to points in a three-dimensional space. Typically, samples from the same class form clusters, whereas those from different classes are isolated (Supplementary Fig. 21). Figure 4h depicts the results showing that the ISOECT array can achieve a prediction accuracy of up to 90%, comparable with conventional artificial neural networks. Remarkably, even after reducing the operating voltage from 400 to 4 mV (Supplementary Fig. 22), ISOECTs were still capable of distinguishing the 16 sequential pulse inputs and maintain a high
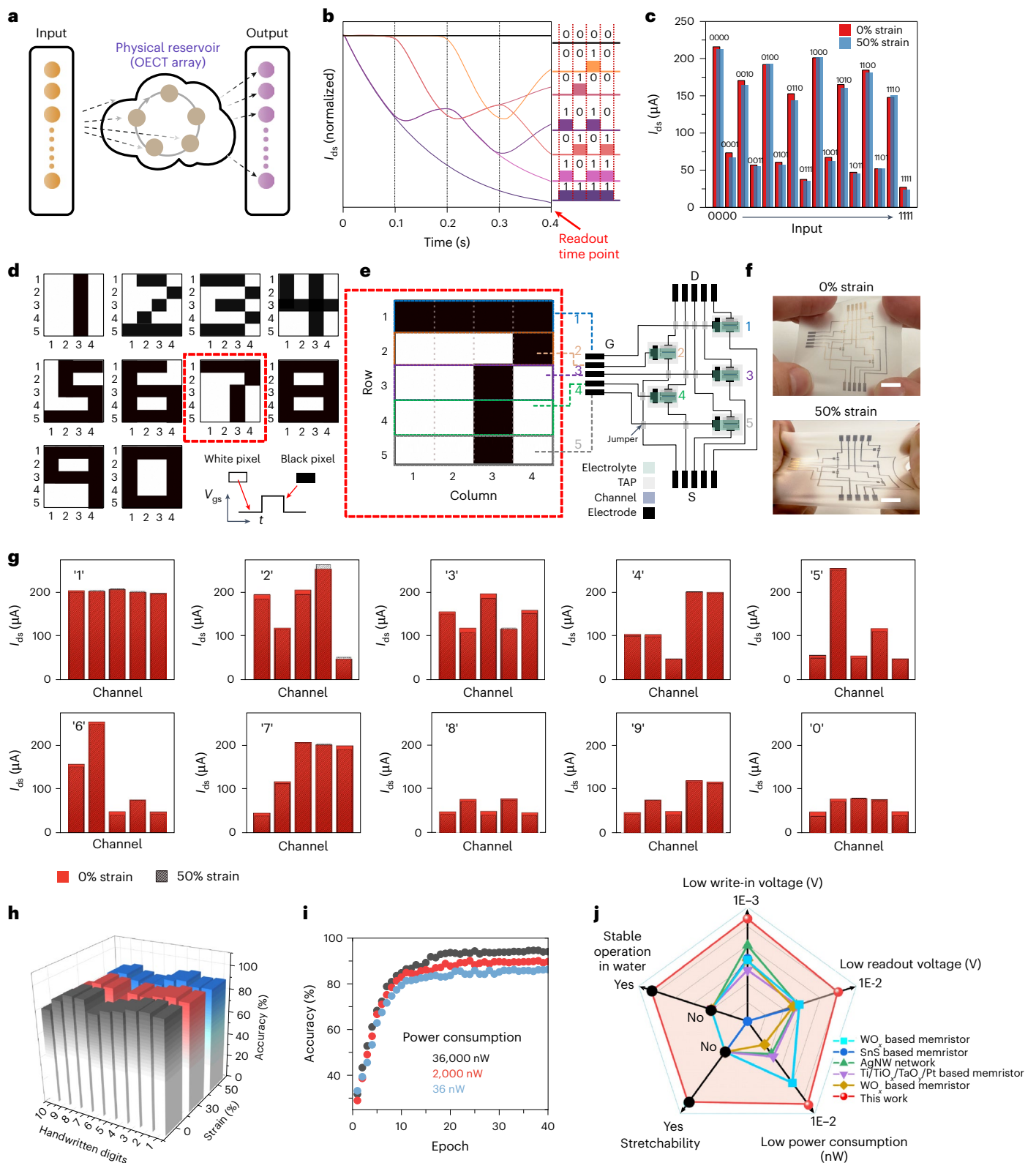
**Fig. 4 | ISOECT array for neuromorphic computing. a**, Schematic of the RC network. **b**, $I_{ds}$ response of ISOECT ($W = 1,000$ μm, $L = 300$ μm) corresponding to different input-pulse combinations ranging from '0000' to '1111'. **c**, Comparison of the determined $I_{ds}$ values at 0% and 50% strain. **d**, Images of the ten digital numbers for RC validation. **e**, Illustration of recognizing the digital number 7 (5 × 4 pixels) with an RC circuit comprising five ISOECTs. The white pixel indicates a low-voltage pulse (0) and the black pixel indicates a high-voltage pulse (1). **f**, Optical images of the ISOECT reservoir circuits at 0% and 50% strain.

Scale bar, 1 cm. **g**, Determined $I_{ds}$ values of ISOECT neurons in the RC circuit on each digital number (from 0 to 9). **h**, Prediction results of handwritten digits using the RC circuit at different strain values (0%, 30% and 50%). **i**, Evolution of the prediction accuracy of ISOECT RC within 40 training epochs. Decreasing the operation voltage ($V_{ds}$) from 400 to 4 mV can reduce the power consumption from 36,000 to 36 nW, without a major compromise on accuracy. **j**, Overall comparison of ISOECT with other common hardware used for RC.
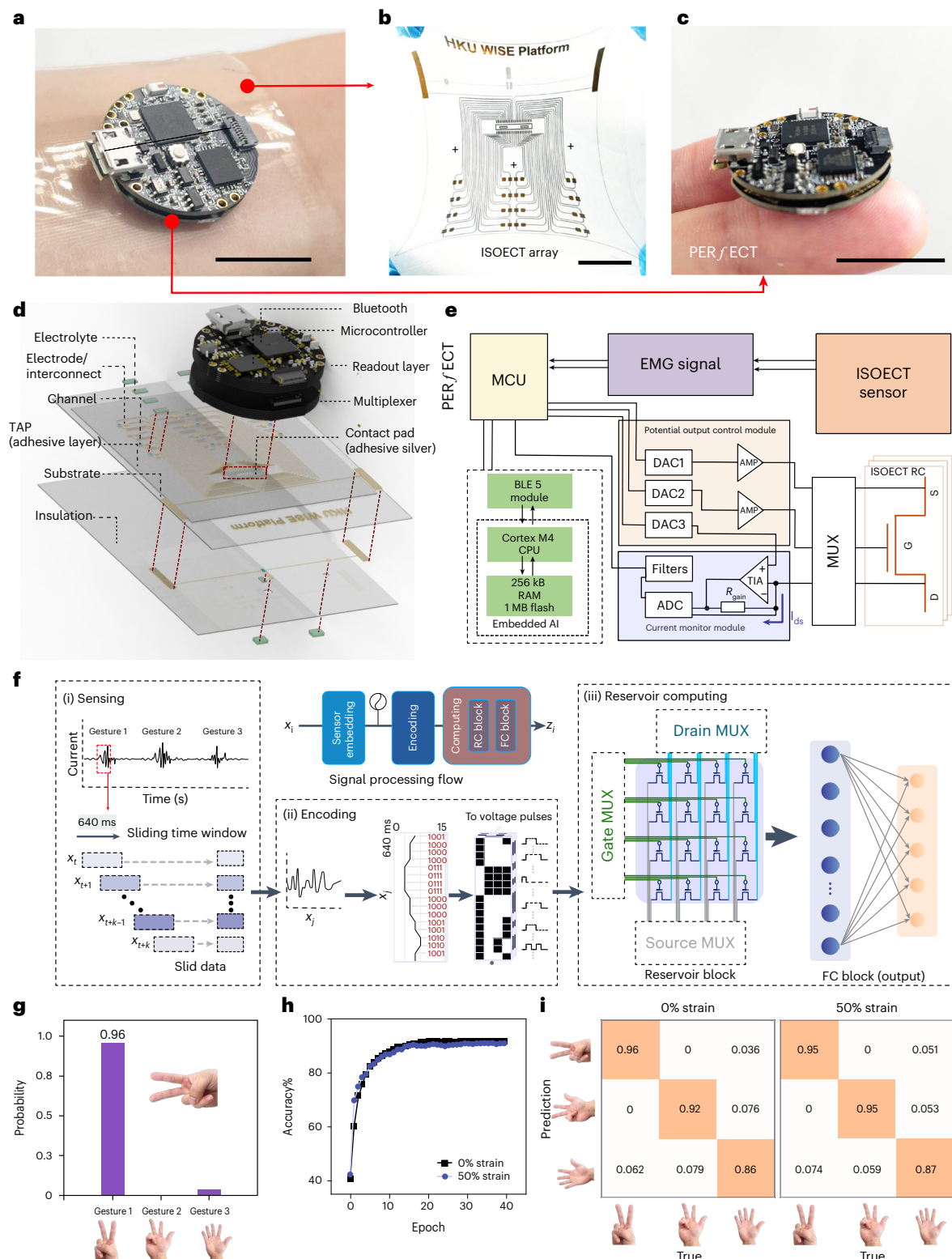
**Fig. 5 | WISE platform for wearable in-sensor computing. a–c**, Optical images of the WISE platform (**a**), the ISOECT array (**b**) and the PERfECT control unit (**c**). Scale bar, 1 cm. **d**, Illustration of the structure of the WISE platform. **e**, Circuit diagram of the WISE platform, including a BLE module, an ISOECT RC array ($W = 500 \, \mu m$, $L = 150 \, \mu m$), analogue front ends, an ISOECT sensor ($W = 500 \, \mu m$, $L = 150 \, \mu m$) and a MCU. BLE, Bluetooth low energy; DAC, digital-to-analog converter; ADC, analog-to-digital converter; AMP, amplifier; MUX, multiplexer; RAM, random-access memory; CPU, central processing unit; MCU, microcontroller unit; TIA, transimpedance amplifier. **f**, Process flow for gesture recognition: (i) preprocessing of EMG signal by sampling with a 640 ms sliding window and a 40 ms stride; (ii) encoding the EMG signals into a stream of voltage pulses (varying between 0000 and 1111); (iii) applying pulses stream (as $V_{gs}$) to ISOECTs and determining $I_{ds}$ readout by using the PERfECT unit, which is subsequently assigned to ISOECT neurons for gesture classification through the fully connected (FC) layer. **g**, Classification accuracy. **h**, Evolution of classification accuracy under 0% and 50% strain. **i**, Comparison of confusion matrices under 0% and 50% strain.

prediction accuracy. The above voltage reduction corresponds to a significant decrease in power consumption from 36,000 to 36 nW (Fig. 4i), demonstrating the energy efficiency of an ISOECT RC network. Figure 4j illustrates, in detail, the advantages of ISOECTs over other technologies. ISOECTs simultaneously achieved low power consumption and mechanical stretchability, an exclusive feature not yet achieved by other RC hardware units[40–44].

## WISE platform for wearable in-sensor computing

The presented protocols for constructing ISOECT arrays and stretchable RC networks open a wide range of applications. As an example, we demonstrate their use for wearable gesture recognition. To enable wearable data acquisition, we combined the arrays with our recently developed coin-sized readout unit, personalized electronic reader for electrochemical transistors (PERfECT) (Supplementary Fig. 23)[45]. The WISE platform uses an ISOECT array for both electromyography (EMG) sensing (leveraging the high $G_m$ value of ISOECTs; Supplementary Fig. 24) and data computing (Fig. 5a–e). The detailed working process is illustrated in Fig. 5f. (1) Sensing: ISOECT sensors detect EMG signals and amplify them at their origin; then, the temporal EMG signals are sampled using a sliding window with a size of 640 ms and a stride of 40 ms. (2) Encoding: the PERfECT system encodes the analogue EMG signals into four-bit sequential voltage pulse streams to feed the ISOECT (Supplementary Fig. 25). (3) The ISOECT array (4 × 4) analysed the input EMG signal sequence, implementing in-sensor RC and yielding the predicted results.

Figure 5g–i demonstrates that the WISE platform can accurately recognize different gestures from EMG signals, with negligible motion artefacts owing to the acquired stretchability. Compared with conventional artificial neural networks, the ISOECT RC unit significantly reduces the memory cost needed for the edge computing of EMG signals that contain complex temporal and sequential information (Supplementary Fig. 26). The ISOECT EMG sensor consumed an energy of approximately 0.035 nJ per operation, whereas the ISOECT RC consumed less than 0.56 nJ. The energy consumption is among the lowest in existing hardware[2,40,42,44,46,47], demonstrating the competitiveness of our platform for practical wearable edge-computing applications.

## Conclusions

We have reported an integrated system for wearable health informatics that is based on ISOECT technologies. To develop our WISE platform, we first established a standardizable material protocol providing intrinsic stretchability to OECTs. To facilitate strain dissipation and mechanical stability, we synthesized an adhesive supramolecular buffer layer (TAP). Subsequently, we developed a multichannel inkjet printing system (six channels), providing one-shot and scalable fabrication of ISOECT arrays with a high yield (>95%) and featured sizes down to 100 µm. Finally, a coin-sized readout unit was developed to provide on-site data processing. As an example, we showed that the WISE platform can be used for the in situ signalling and analysis of EMG, offering high prediction accuracy (~90%) for wearable gesture recognition.

By focusing on a system engineering approach and solving compatibility issues between parts of the device, we have been able to show the potential of ISOECTs in practical on-body wearable applications. ISOECTs combine low-voltage operation (<1 V), high $G_m$ and good mechanical properties, making them advantageous for biosensing, and their low-cost and scalable fabrication makes them well suited to wearable applications.

Here we used depletion-mode PEDOT:PSS OECTs due to their high stability and reliability. However, to deliver lower standby power and facilitate further scaling, enhancement-mode ISOECTs will be needed. There is also the potential to improve the frequency response of ISOECTs. Compared with their rigid counterparts, ISOECTs are relatively slow due to the use of ion gels with slow ion transport. Our ISOECTs with a channel length of 100 µm can achieve cutoff frequencies between $10^2$ and $10^3$ Hz, sufficient to cover a range of electrophysiological signals. Further improvements in frequency response could be achieved by optimizing the device structure or adjusting the operating voltages[48,49].

## Methods

### Materials

PEDOT:PSS aqueous suspension (Clevios PH1000) was purchased from Heraeus Electronic Material. PAA (average $M_w$ = 2,000), PEGDE (average $M_n$ = 500), glycerol, dodecylbenzene sulfonic acid (DBSA), sodium chloride and ammonium persulfate were purchased from Sigma-Aldrich. SEBS compounds H1221 with poly(ethylene-co-butylene) volume fractions of 88% were provided by Asahi Kasei. Toluene, PAA (average $M_w$ = 250,000), zwitterionic monomer 3-dimethyl(methacryloyloxy ethyl) ammonium propane sulfonate, 2,2-bis(hydroxymethyl)propionic acid (DMPA, 98%), 2,2-dimethoxypropane (DMP, 98%), sodium chloride (NaCl, ≥99.5%), sodium bicarbonate (NaHCO₃, ≥99.8%), N-hydroxysuccinimide (NHS, 98%), N-(3-dimethylaminopropyl)-N'-ethylcarbodiimide hydrochloride (EDC-HCl, 98.5%), methanol, dichloromethane (DCM), hydrochloric acid (36%–38%) and acetone were obtained from Aladdin. Dopamine hydrochloride (DA-HCl, 98%), polyteramethylene glycol ($M_n$ = 1,000), dibutyltin dilaurate (95%), toluenesulfonic acid, isophorone diisocyanate, trifluoroacetic acid, dibutyltin dilaurate and 1,4-butanediol were purchased from Sigma-Aldrich and dried under a vacuum before use. 1-Ethyl-3-methylimidazolium ethyl sulfate was obtained from TCI. The ink of silver nanowires (2–5 µm, 10 mg ml⁻¹) was purchased from Haitai Naxin Technology. The Au ink (JG-125, 25 mg ml⁻¹) was purchased from Novacentrix.

### Preparation of PEDOT:PSS mixtures

PEDOT:PSS aqueous suspension was first stirred for 3 min and then diluted with water with a 1:1 volume ratio. Then, the diluted mixture was mixed with glycerol (5 v/v%), GOPS (0.05 v/v%), PEGDE (0.2 v/v%) and DBSA (0.25 v/v%) with a vortex mixer (MX-S). The dilution process facilitated the process of inkjet printing and prevented aggregation on the print head. The addition of glycerol increases the film conductivity. DBSA was added to facilitate the wetting property of films on substrates. GOPS or PEGDE was added to crosslink PEDOT:PSS. Then, the mixed suspension was filtered with a polytetrafluoroethylene membrane (aperture size, 0.22 µm) to remove aggregates for further use.

### Synthesis of TAP

The synthesis of TAP according to previously reported methods[50] is listed below.

i.   Synthesis of DMP-DMPA. DMPA (100 mmol) and DMP (130 mmol) were dissolved in 100 ml acetone, and then 0.1 g toluenesulfonic acid (0.53 mmol) was added at room temperature for a 4 h reaction. Then, 50 mmol NaHCO₃ was added to neutralize the solution and stirred for an additional 20 min; the residual solid was removed by filtration. Then, the crude product was dried and dissolved in DCM. Finally, after drying under 50 °C overnight, DMP-DMPA was obtained.

ii.  Synthesis of DMP-DMPA-NHS. DMP-DMPA (50 mmol) and NHS (60 mmol) were added into a 500 ml single-necked flask, and dissolved by 200 ml DCM. Then, EDC-HCl (120 mmol) was added and stirred for 2.5 h at 0 °C and 20 h at room temperature for reaction. Then, the crude product was washed with saturated NaHCO₃ solution, dilute hydrochloric acid solution and water. Anhydrous sodium sulfate was used to remove the residue water in organic phase. After filtration and drying overnight at 60 °C in a vacuum, the white solid product (DMP-DMPA-NHS) was obtained.

iii. Synthesis of DMP-DMPA-DA. DA-HCl (30 mmol) was added to a 250 ml three-necked flask under a nitrogen atmosphere and

then dissolved in a mixture of 70 ml DCM and 70 ml methanol. DMP-DMPA-NHS (20 mmol) was then added for the reaction and stirred at 0 °C for 20 h. After the solvent evaporation, a yellow viscous material was obtained. Then, the material was washed with a dilute hydrochloric acid solution. DMP-DMPA-DA can then be obtained by collecting the white precipitate and dried at 50 °C in a vacuum overnight.

iv. Synthesis of DMPA-DA. In a 150 ml three-necked flask under a nitrogen atmosphere, 15 mmol DMP-DMPA-DA was added. Then, 100 ml methanol and 15 mmol trifluoroacetic acid were added and stirred at room temperature for 16 h. After that, the crude product was obtained by filtration, and concentrated in a vacuum. Finally, DMPA-DA was obtained by drying at 50 °C overnight in a vacuum.

v. Synthesis of TAP. In a three-necked flask equipped with a mechanical stirrer under nitrogen, add two molar equivalents of isophorone diisocyanate and dibutyltin dilaurate. Then, add one molar equivalent of polyteramethylene glycol and stir at 75 °C for 3.5 h. DMPA-DA and 1,4-butylene glycol were then added to the prepolymer and stirred at 85 °C for 4 h. Then, the reactant was poured into a polytetrafluoroethylene plate and placed in an oven at 50 °C overnight to complete the reaction.

### Synthesis of stretchable gel
First, zwitterionic monomer 3-dimethyl(methacryloyloxyethyl) ammonium propane sulfonate was mixed with an IL (with a molar ratio of 1:1.25) and then initiated by ammonium persulfate (0.2 mol%) in a PAA aqueous solution. The molar ratio of the monomer units of PAA and PDMAPS was fixed at 1:1, and the monomer concentration during polymerization is 30 wt%. The polymerization proceeded at 80 °C for 6 h under nitrogen protection. In the final samples after being dried, the molar ratio of PDMAPS, PAA and IL is 1:1:1.25.

### Fabrication of the ISOECT array
For ISOECT devices, the stretchable substrate was fabricated by casting a SEBS solution (10 w/w% in toluene) in a glass Petri dish, followed by solvent evaporation in a fume hood under room temperature for 2 days. Then, the patterning of the functional layer was based on our customized multichannel inkjet printer. First, the stretchable substrate was thoroughly cleaned with ethanol and deionized water and completely dried before the next step. Cleaned substrates were treated with an ultraviolet–ozone cleaner for 10 min. Immediately after this treatment, a layer of TAP was patterned by inkjet printing the ink (1 w/w% in EtOH (80%)/butyl acetate (20%) solution), followed by 30 min of baking at 60 °C to cure the buffer layer. Then, stretchable electrodes were patterned by vapour deposition of nano Au (20 nm) through an in situ printed water-soluble shadow mask (PAA; average $M_w$ = 2,000), followed by water development. A firm positioning fixture was customized on the printing platform for sample repositioning. In the area of interconnects, a layer of silver nanowires was printed on top to guarantee conductivity under strain. After that, PEDOT:PSS was printed between the S and D electrodes as the channel, followed by baking at 100 °C for 30 min. Afterwards, a layer of TAP was printed on the S and D electrodes as insulation to minimize the leakage current. In the end, the electrolyte was printed to connect the gate and channel. After curing at room temperature overnight, the architecture of the OECT can be completed.

### Characterization
The electrical performance of the PEDOT:PSS film was measured using Agilent B2900A controlled with Python software (Windows 64-bit 3.10). The strain test of the film was performed with a tensile machine (Feinixs, FMSXX 80-50-50). The cracking of the PEDOT:PSS film under strain was studied with a Nikon optical microscope. For transistor characterization, the transfer, output and transient responses were measured with a customized wearable characterization device, that is, PERfECT. Details can be found in our previous work[45].

### Simulations
The single fully connected (FC) perceptron layer was used to fit the weights of the output layer. The cross-entropy loss is minimized by batch gradient descent using the adaptive momentum estimations (learning ratio, 0.01) optimizer. The accuracies of the handwriting classification were obtained as follows: the current flowing through the ISOECT device in the reservoir at the final time step was used as the input to the output layer. The cross-entropy loss was minimized by a mini-batch gradient descent using the Adam optimizer (learning rate, 0.001).

### Electrical component
The circuit diagram of PERfECT was designed using open-access electronic design automation software (LCEDA, lceda pro-windows-x64-2.2.27.1). The printed circuit board (PCB) of PERfECT was fabricated by a commercial PCB manufacturer (JLCPCB). All these electronic and analytical components were ordered from DigiKey and then integrated into the PCB. Customized assembly of these units was carried out in cooperation with SESIC. The circuit was programmed using the Joint Test Action Group interface, and the circuit firmware was developed in C language (C11/C18). A multilayer fabrication process was used to reduce the size of the PCBs. More details about the readout system can be found in our previous work[45]. To ensure the sustained and reliable operation of the entire system, a rechargeable lithium polymer battery was used as the power source. The battery was connected to a low-dropout linear voltage regulator (ADP7112, Analog Devices), which effectively regulates and supplies a stable voltage output. The local processing relies on a Bluetooth Low Energy (BLE) system-on-a-chip (nRF52840-CKAA, Nordic Semiconductor). This multifunctional component serves as the Bluetooth communication module and facilitates the storage and execution of the final output layer of the RC network. For wireless data transmission, the BLE system-on-a-chip uses a miniature ceramic antenna operating at 2.45 GHz.

Then, to implement RC into the wearable gesture recognition system, the design and deployment of the final FC layer requires careful considerations to better balance the computational power consumption and accuracy. To train and obtain the weights inside the FC layer, pre-collected EMG data were randomly divided into three datasets: 60% for training, 20% for validation and 20% for testing. Considering the limited data storage space and computational power, the model parameters were then frozen and quantized, resulting in an eight-bit network with a reduced size of less than 20 kB. Finally, the quantized FC layer was transformed into a C array format, enabling compilation into the system-on-a-chip program.

### Reporting summary
Further information on research design is available in the Nature Portfolio Reporting Summary linked to this article.

## Data availability
Data that support the findings of this study are available from the corresponding authors upon reasonable request.

## Code availability
The code used for RC is available via GitHub at https://github.com/HKU-WISE-Group/OECT-RC.

## References
1. Xu, C., Solomon, S. A. & Gao, W. Artificial intelligence-powered electronic skin. *Nat. Mach. Intell.* **5**, 1344–1355 (2023).
2. Moin, A. et al. A wearable biosensing system with in-sensor adaptive machine learning for hand gesture recognition. *Nat. Electron.* **4**, 54–63 (2021).

3.  Hartmann, M., Hashmi, U. S. & Imran, A. Edge computing in smart health care systems: review, challenges, and research directions. *Trans. Emerging Tel. Techn.* **33**, e3710 (2022).

4.  Dai, S. et al. Intrinsically stretchable neuromorphic devices for on-body processing of health data with artificial intelligence. *Matter* **5**, 3375–3390 (2022).

5.  Wan, T. et al. In-sensor computing: materials, devices, and integration technologies. *Adv. Mater.* **35**, 2203830 (2023).

6.  Zhou, F. & Chai, Y. Near-sensor and in-sensor computing. *Nat. Electron.* **3**, 664–671 (2020).

7.  Dai, Y., Hu, H., Wang, M., Xu, J. & Wang, S. Stretchable transistors and functional circuits for human-integrated electronics. *Nat. Electron.* **4**, 17–29 (2021).

8.  Kim, H.-J., Sim, K., Thukral, A. & Yu, C. Rubbery electronics and sensors from intrinsically stretchable elastomeric composites of semiconductors and conductors. *Sci. Adv.* **3**, e1701114 (2017).

9.  Guan, Y.-S. et al. Elastic electronics based on micromesh-structured rubbery semiconductor films. *Nat. Electron.* **5**, 881–892 (2022).

10. Khodagholy, D. et al. In vivo recordings of brain activity using organic transistors. *Nat. Commun.* **4**, 1575 (2013).

11. Van De Burgt, Y. et al. A non-volatile organic electrochemical device as a low-voltage artificial synapse for neuromorphic computing. *Nat. Mater.* **16**, 414–418 (2017).

12. Gkoupidenis, P., Schaefer, N., Strakosas, X., Fairfield, J. A. & Malliaras, G. G. Synaptic plasticity functions in an organic electrochemical transistor. *Appl. Phys. Lett.* **107**, 263302 (2015).

13. Wang, S. et al. An organic electrochemical transistor for multi-modal sensing, memory and processing. *Nat. Electron.* **6**, 281–291 (2023).

14. Rivnay, J. et al. Organic electrochemical transistors. *Nat. Rev. Mater.* **3**, 17086 (2018).

15. Oldroyd, P., Gurke, J. & Malliaras, G. G. Stability of thin film neuromodulation electrodes under accelerated aging conditions. *Adv. Funct. Mater.* **33**, 2208881 (2023).

16. Liu, Y. et al. Morphing electronics enable neuromodulation in growing tissue. *Nat. Biotechnol.* **38**, 1031–1036 (2020).

17. Bai, J. et al. Coin-sized, fully integrated, and minimally invasive continuous glucose monitoring system based on organic electrochemical transistors. *Sci. Adv.* **10**, eadl1856 (2024).

18. Bai, J., Liu, D., Tian, X. & Zhang, S. Tissue-like organic electrochemical transistors. *J. Mater. Chem. C* **10**, 13303–13311 (2022).

19. Li, N. et al. Bioadhesive polymer semiconductors and transistors for intimate biointerfaces. *Science* **381**, 686–693 (2023).

20. Wu, X. et al. Universal spray-deposition process for scalable, high-performance, and stable organic electrochemical transistors. *ACS Appl. Mater. Interfaces* **12**, 20757–20764 (2020).

21. Zhang, S. et al. Tuning the electromechanical properties of PEDOT:PSS films for stretchable transistors and pressure sensors. *Adv. Electron. Mater.* **5**, 1900191 (2019).

22. Zhang, S. et al. Patterning of stretchable organic electrochemical transistors. *Chem. Mater.* **29**, 3126–3132 (2017).

23. Marchiori, B., Delattre, R., Hannah, S., Blayac, S. & Ramuz, M. Laser-patterned metallic interconnections for all stretchable organic electrochemical transistors. *Sci. Rep.* **8**, 8477 (2018).

24. Boda, U., Petsagkourakis, I., Beni, V., Andersson Ersman, P. & Tybrandt, K. Fully screen-printed stretchable organic electrochemical transistors. *Adv. Mater. Technol.* **8**, 2300247 (2023).

25. Chen, J. et al. Highly stretchable organic electrochemical transistors with strain-resistant performance. *Nat. Mater.* **21**, 564–571 (2022).

26. Lee, W. et al. Nonthrombogenic, stretchable, active multielectrode array for electroanatomical mapping. *Sci. Adv.* **4**, eaau2426 (2018).

27. Li, Y., Wang, N., Yang, A., Ling, H. & Yan, F. Biomimicking stretchable organic electrochemical transistor. *Adv. Electron. Mater.* **5**, 1900566 (2019).

28. Zhong, D. et al. High-speed and large-scale intrinsically stretchable integrated circuits. *Nature* **627**, 313–320 (2024).

29. Liu, D. et al. Intrinsically stretchable organic electrochemical transistors with rigid-device-benchmarkable performance. *Adv. Sci.* **9**, 2203418 (2022).

30. Lacour, S. P., Chan, D., Wagner, S., Li, T. & Suo, Z. Mechanisms of reversible stretchability of thin metal films on elastomeric substrates. *Appl. Phys. Lett.* **88**, 204103 (2006).

31. Paulsen, B. D., Tybrandt, K., Stavrinidou, E. & Rivnay, J. Organic mixed ionic–electronic conductors. *Nat. Mater.* **19**, 13–26 (2020).

32. Kindaichi, S., Matsubara, R., Kubono, A., Yamamoto, S. & Mitsuishi, M. Preparation of resilient organic electrochemical transistors based on blend films with flexible crosslinkers. Preprint at https://chemrxiv.org/engage/chemrxiv-article-details/6441ed8fe4b bbe4bbffc4bb0 (2023).

33. Kang, J. et al. Tough-interface-enabled stretchable electronics using non-stretchable polymer semiconductors and conductors. *Nat. Nanotechnol.* **17**, 1265–1271 (2022).

34. Lei, Z. & Wu, P. A highly transparent and ultra-stretchable conductor with stable conductivity during large deformation. *Nat. Commun.* **10**, 3429 (2019).

35. Appeltant, L. et al. Information processing using a single dynamical node as complex system. *Nat. Commun.* **2**, 468 (2011).

36. Ji, X. et al. Mimicking associative learning using an ion-trapping non-volatile synaptic organic electrochemical transistor. *Nat. Commun.* **12**, 2480 (2021).

37. Liang, X., Luo, Y., Pei, Y., Wang, M. & Liu, C. Multimode transistors and neural networks based on ion-dynamic capacitance. *Nat. Electron.* **5**, 859–869 (2022).

38. Paudel, P. R., Skowrons, M., Dahal, D., Radha Krishnan, R. K. & Lüssem, B. The transient response of organic electrochemical transistors. *Adv. Theory Simul.* **5**, 2100563 (2022).

39. Friedlein, J. T., McLeod, R. R. & Rivnay, J. Device physics of organic electrochemical transistors. *Org. Electron.* **63**, 398–414 (2018).

40. Du, C. et al. Reservoir computing using dynamic memristors for temporal information processing. *Nat. Commun.* **8**, 2204 (2017).

41. Sun, L. et al. In-sensor reservoir computing for language learning via two-dimensional memristors. *Sci. Adv.* **7**, eabg1455 (2021).

42. Milano, G. et al. *In materia* reservoir computing with a fully memristive architecture based on self-organizing nanowire networks. *Nat. Mater.* **21**, 195–202 (2022).

43. Zhong, Y. et al. Dynamic memristor-based reservoir computing for high-efficiency temporal signal processing. *Nat. Commun.* **12**, 408 (2021).

44. Moon, J. et al. Temporal data classification and forecasting using a memristor-based reservoir computing system. *Nat. Electron.* **2**, 480–487 (2019).

45. Tian, X. et al. Pushing OECTs toward wearable: development of a miniaturized analytical control unit for wireless device characterization. *Anal. Chem.* **94**, 6156–6162 (2022).

46. Kim, K. K. et al. A substrate-less nanomesh receptor with meta-learning for rapid hand task recognition. *Nat. Electron.* **6**, 64–75 (2023).

47. Cucchi, M. et al. Reservoir computing with biocompatible organic electrochemical networks for brain-inspired biosignal classification. *Sci. Adv.* **7**, eabh0693 (2021).

48. Spyropoulos, G. D., Gelinas, J. N. & Khodagholy, D. Internal ion-gated organic electrochemical transistor: a building block for integrated bioelectronics. *Sci. Adv.* **5**, eaau7378 (2019).

49. Friedlein, J. T., Donahue, M. J., Shaheen, S. E., Malliaras, G. G. & McLeod, R. R. Microsecond response in organic electrochemical transistors: exceeding the ionic speed limit. *Adv. Mater.* **28**, 8398–8404 (2016).

50. Xu, Z. et al. A highly-adhesive and self-healing elastomer for bio-interfacial electrode. *Adv. Funct. Mater.* **31**, 2006432 (2021).

## Acknowledgements

## Author contributions

S.Z., Z.W. and D.L. conceived the idea. S.Z. acquired funding and supervised the whole research. D.L., X.T., J.B. and S.W. conducted the experiments and collected the data. X.T., J.B. and S.W. contributed to the algorithm design and simulation. S.Z., X.T. and J.B. designed the PERfECT readout system for wearable data analysis. X.T. and J.B. coded the AI-embedded program in PERfECT for in-sensor computing with an ISOECT array. D.L., X.T., J.B. and Y.W. contributed to the fabrication of the ISOECT array. D.L., X.T., Y.W. and S.D. contributed to the ISOECT device characterization. S.Z. and D.L. drafted the manuscript. All authors contributed to revising the manuscript.

## Competing interests

The authors declare no competing interests.

## Additional information

**Supplementary information** The online version contains supplementary material available at https://doi.org/10.1038/s41928-024-01250-9.

**Correspondence and requests for materials** should be addressed to Zhongrui Wang or Shiming Zhang.

**Peer review information** *Nature Electronics* thanks Sahika Inal and the other, anonymous, reviewer(s) for their contribution to the peer review of this work.

**Reprints and permissions information** is available at www.nature.com/reprints.

Corresponding author(s): Shiming Zhang, Zhongrui Wang

Last updated by author(s): Jul 18, 2024

# Reporting Summary

Nature Portfolio wishes to improve the reproducibility of the work that we publish. This form provides structure for consistency and transparency in reporting. For further information on Nature Portfolio policies, see our Editorial Policies and the Editorial Policy Checklist.

## Statistics

For all statistical analyses, confirm that the following items are present in the figure legend, table legend, main text, or Methods section.

| n/a | Confirmed | |
|---|---|---|
| ☐ | ☒ | The exact sample size (*n*) for each experimental group/condition, given as a discrete number and unit of measurement |
| ☐ | ☒ | A statement on whether measurements were taken from distinct samples or whether the same sample was measured repeatedly |
| ☐ | ☒ | The statistical test(s) used AND whether they are one- or two-sided<br>*Only common tests should be described solely by name; describe more complex techniques in the Methods section.* |
| ☐ | ☒ | A description of all covariates tested |
| ☐ | ☒ | A description of any assumptions or corrections, such as tests of normality and adjustment for multiple comparisons |
| ☐ | ☒ | A full description of the statistical parameters including central tendency (e.g. means) or other basic estimates (e.g. regression coefficient) AND variation (e.g. standard deviation) or associated estimates of uncertainty (e.g. confidence intervals) |
| ☒ | ☐ | For null hypothesis testing, the test statistic (e.g. *F*, *t*, *r*) with confidence intervals, effect sizes, degrees of freedom and *P* value noted<br>*Give P values as exact values whenever suitable.* |
| ☒ | ☐ | For Bayesian analysis, information on the choice of priors and Markov chain Monte Carlo settings |
| ☒ | ☐ | For hierarchical and complex designs, identification of the appropriate level for tests and full reporting of outcomes |
| ☒ | ☐ | Estimates of effect sizes (e.g. Cohen's *d*, Pearson's *r*), indicating how they were calculated |

*Our web collection on statistics for biologists contains articles on many of the points above.*

## Software and code

Policy information about availability of computer code

| | |
|---|---|
| Data collection | Agilent Keithley B2902A (Keysight B2900 Quick IV Measurement Software). PERfECT Measurement System (DOI: 10.1021/acs.analchem.1c05210) |
| Data analysis | Origin 2018. Matlab 2016b. Python 3.8. |

For manuscripts utilizing custom algorithms or software that are central to the research but not yet described in published literature, software must be made available to editors and reviewers. We strongly encourage code deposition in a community repository (e.g. GitHub). See the Nature Portfolio guidelines for submitting code & software for further information.

## Data

Policy information about availability of data

All manuscripts must include a data availability statement. This statement should provide the following information, where applicable:
- Accession codes, unique identifiers, or web links for publicly available datasets
- A description of any restrictions on data availability
- For clinical datasets or third party data, please ensure that the statement adheres to our policy

All data supporting the findings of this study are available within the Article and its Supplementary Information. Additional raw data generated in this study are available from the corresponding authors upon reasonable request.

# Human research participants

Policy information about studies involving human research participants and Sex and Gender in Research.

| | |
|---|---|
| Reporting on sex and gender | N/A |
| Population characteristics | N/A |
| Recruitment | N/A |
| Ethics oversight | N/A |

Note that full information on the approval of the study protocol must also be provided in the manuscript.

# Field-specific reporting

Please select the one below that is the best fit for your research. If you are not sure, read the appropriate sections before making your selection.

☐ Life sciences     ☐ Behavioural & social sciences     ☐ Ecological, evolutionary & environmental sciences

For a reference copy of the document with all sections, see nature.com/documents/nr-reporting-summary-flat.pdf

# Life sciences study design

All studies must disclose on these points even when the disclosure is negative.

| | |
|---|---|
| Sample size | N/A |
| Data exclusions | N/A |
| Replication | N/A |
| Randomization | N/A |
| Blinding | N/A |

# Behavioural & social sciences study design

All studies must disclose on these points even when the disclosure is negative.

| | |
|---|---|
| Study description | N/A |
| Research sample | N/A |
| Sampling strategy | N/A |
| Data collection | N/A |
| Timing | N/A |
| Data exclusions | N/A |
| Non-participation | N/A |
| Randomization | N/A |

# Ecological, evolutionary & environmental sciences study design

All studies must disclose on these points even when the disclosure is negative.

| | |
|---|---|
| Study description | N/A |
| Research sample | N/A |
| Sampling strategy | N/A |
| Data collection | N/A |
| Timing and spatial scale | N/A |
| Data exclusions | N/A |
| Reproducibility | N/A |
| Randomization | N/A |
| Blinding | N/A |

Did the study involve field work? ☐ Yes ☒ No

# Reporting for specific materials, systems and methods

We require information from authors about some types of materials, experimental systems and methods used in many studies. Here, indicate whether each material, system or method listed is relevant to your study. If you are not sure if a list item applies to your research, read the appropriate section before selecting a response.

## Materials & experimental systems

| n/a | Involved in the study |
|---|---|
| ☒ ☐ | Antibodies |
| ☒ ☐ | Eukaryotic cell lines |
| ☒ ☐ | Palaeontology and archaeology |
| ☒ ☐ | Animals and other organisms |
| ☒ ☐ | Clinical data |
| ☒ ☐ | Dual use research of concern |

## Methods

| n/a | Involved in the study |
|---|---|
| ☒ ☐ | ChIP-seq |
| ☒ ☐ | Flow cytometry |
| ☒ ☐ | MRI-based neuroimaging |